Topology optimization method for the design of bioinspired self-similar hierarchical microstructures

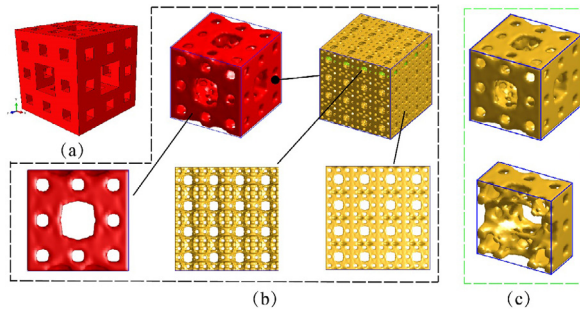Hui-Kai Zhang[a], Wen-Jun Wu[b], Zhan Kang[b], Xi-Qiao Feng[a],*

[a] *Institute of Biomechanics and Medical Engineering, AML, Department of Engineering Mechanics, Tsinghua University, Beijing 100084, China*
[b] *Department of Engineering Mechanics, Dalian University of Technology, Dalian 116024, China*

Graphical Abstract

A concurrent topology optimization method is developed for designing fractal structures by introducing the Boolean subtraction operator (BSO) to guarantee the self-similarity of geometry at different levels.

Abstract

Design of fractal microstructures holds promise for developing advanced materials with improved mechanical properties and multiple functions. In this paper, a concurrent topology optimization method is proposed to design both two- and three-dimensional, fractal or hierarchical microstructures. The Boolean subtraction operator (BSO) is introduced to guarantee the self-similarity among a hierarchical structure at different levels. This method allows us to generate a diversity of fractal structures which have, for instance, the geometric feature of either clockwise or counterclockwise chirality. By evoking the fractal Menger sponge as the non-designed domain, we have obtained fractal structures in which all internal transversal sections have hybrid fractal morphologies. Though our attention is here focused only on the mechanical properties of materials, the proposed method can also be applied to design fractal structures with optimal optical, acoustic, and electromagnetic properties.
© 2020 Elsevier B.V. All rights reserved.

---

* Corresponding author.
 E-mail address: fengxq@tsinghua.edu.cn (X.Q. Feng).

1. Introduction

The concept of fractal, initiated by Mandelbrot, describes the scale-invariant feature of self-similar geometric patterns. Fractal patterns are ubiquitous in nature, such as blood vessels and coastlines [1]. For a coastline, for example, its reduced-scale structure usually exhibits a certain similarity to the whole geometry, and the measured length of the coastline becomes larger when a finer scale is used. When the number of fractal order increases one time, the length of the curve increases about 4/3 times for a curve with the fractal dimension of 4/3 [1]. In nature, fractal structures can provide a larger space, which is beneficial for the habitation of microbes [2].

Self-similar structural hierarchy is a prominent feature of most live biological systems, e.g., neurosciences [3], cancer cell nuclei [4], brain glial cells [5], myelin membrane monolayers [6], and coronary arteries and veins [7]. Hierarchical structures play a significant role in the regulation of their mechanical properties and biological functions. For example, hierarchical surface structures endow many biological materials with superhydrophobicity-based functions, e.g., self-cleaning and antifogging [8]. Interestingly, Rosetti et al. [6] found that the fractal surface patterns of myelin membrane monolayers are dependent on the internal pressure. In plants, leaf veins, snowflakes and Roman cauliflower have different fractal or hierarchical morphologies. For example, Roman cauliflowers have several orders of self-similar helical structures, each consisting of a number of chiral unit blocks with smaller characteristic sizes (Fig. 1).

Materials with self-similar hierarchical structures have also found many technologically significant applications in engineering, e.g., absorbing structures [9–11], acoustic and electromagnetic metamaterials [12–16], and composite structures [17–20]. For example, Zhang et al. [21] and Fan et al. [22] used fractal networks to design stretchable flexible electronics, which can meet the demand to the large coverage area of functional electronics. Meza et al. [23] and Zheng et al. [24] used the microstereolithography technique to fabricate three-dimensional (3D) hierarchical lattice structures, in which stretch- and bend-dominated self-similar structures are assembled. Recently, 3D fractal multi-vascular networks and functional intravascular topologies made of biocompatible hydrogels are designed and printed by using the stereolithography method [25]. In the 3D printing technique of vascular networks, fractal mathematics can guarantee that the second-order vascular architecture does not intersect the first-order structure. In addition, materials with fractal geometry have also attracted much attention in the field of medical engineering, thanks to their analogy to such biological tissues as bones and muscles [26].

In recent years, much effort has been directed toward designing self-similar hierarchical structures on the basis of classical mathematical fractal graphics, such as Koch curve [11] and snowflake. It has been demonstrated that these fractal structures can be used to achieve some improved mechanical, acoustic, and electromagnetic properties. However, there is still a lack of an efficient method to design hierarchical structures with desired properties and functions.

The topology optimization method [27–30] has widely been invoked to design the microstructures of materials [31]. In particular, concurrent topology optimization schemes have been developed for designing both the first- and second-level structures consisting of different unit blocks [32–34]. The effective elastic property of materials in the optimized first-level microstructure can be estimated by the micromechanical homogenization theory [35–37].

To guarantee the geometric self-similarity between the first- and second-level structures, in the present paper, we introduce the Boolean subtraction operator (BSO) in the concurrent topology optimization framework. BSO serves as an effective constraint for correlating the optimized first- and second-level structures. In comparison with fractal structures previously designed in the literature, the method proposed in this paper is operated through optimization iterations starting from one random initial topology, which can not only enhance the design space but also achieve some exotic 2D or 3D unpredictable designs with prescribed functions.

This paper is organized as follows: The Boolean subtraction operator is introduced in Section 2. In Section 3, the two-level topology optimization framework of the problem is established on the basis of the BSO, and the adjoint sensitivity analysis is implemented. In Section 4, we validate the efficacy of the Boolean constraint method, and some 2D and 3D fractal structures subjected to multiple loads are provided to demonstrate the proposed scheme. In particular, we introduce the fractal Menger Sponge as one non-designed domain into the concurrent optimization design. The main conclusions drawn from this study are summarized in Section 5.

2. Boolean subtraction operator

Fractal or hierarchical structures are ubiquitous in biological materials. For instance, Fig. 1 shows the fractal architecture of a Roman cauliflower, in which the structure at one length scale shown in Fig. 1(a) is composed of
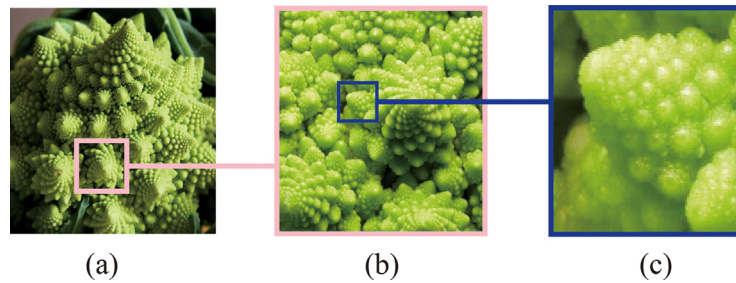
Fig. 1. Self-similar fractal geometry of Roman cauliflower: (a) the third-order structure, (b) the second-order structure, and (c) the first-order structure.
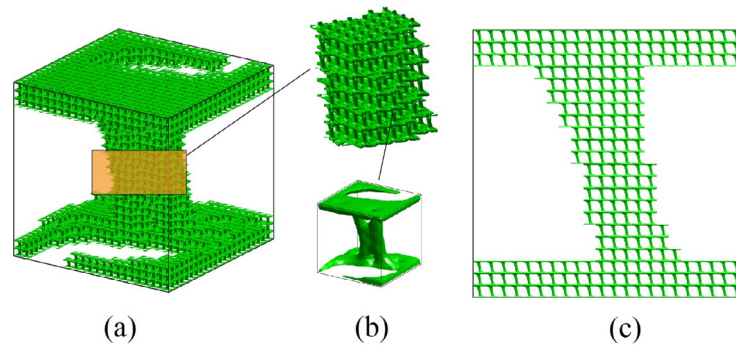

Fig. 2. Schematic diagram of a fractal structures: (a) macrostructure, (b) the side view of the microstructure, and (c) the right view of the magnified microstructure.

a number of smaller unit cells (Fig. 1b), and the geometric properties at different length scales are quite similar (Fig. 1c). Inspired by such biological materials, we will develop a concurrent topology optimization scheme to design self-similar or fractal hierarchical structures, as shown in Fig. 2. In spite of previous attempts to design hierarchical structures by topology optimization methods, it remains unclear how to ensure the self-similarity of the hierarchical structures at different length scales.

For this purpose, we first introduce the Boolean subtraction operator (BSO) [38,39]. In Fig. 3, structure-A without internal topological structure is defined as the reference configuration. Structure-B and structure-C1, C2 and C3 with different topologies are shown in Fig. 3(b) and (c), respectively. The Boolean subtraction operator 'B–C' is defined in the sense that the object B is subtracted by the part coinciding with the object C. For illustration, Fig. 3(c) shows three types of object C, referred to as structure-C1, C2 and C3, respectively. Among them, structure-C1 has the opposite topology to structure-B, and thus the operation of 'B–C1' leads to the structure-D1 shown in Fig. 3(d), which is identical to structure-B. The second structure, C2, has different internal void topology from the structure-B, and the operation of 'B–C2' yields a more complex structure-D2. In addition, if structure-C3 is the same as structure-B, and we can also obtain the null set as structure-D3. Using the BSO defined above, it is expected that the final optimized structures at different levels have the same topology, and the result of BSO is null like the case of 'B–C3'. This design principle will be formulated in what follows and demonstrated by a number of examples.

In voxel topology methods, such as the solid interpolation material penalty (SIMP) method [27,28], both the square macrostructure shown in Fig. 4(a) and its square microstructure (unit cells) shown in Fig. 4(b) are discretized into N mesh elements. Let Ω^0 and Ω^* denote the design domains of macrostructure and microstructure, respectively. To describe the material layouts of the two-level structures, we introduce the macroscale design variables $x_i^0 \in [0, 1]$. $(i = 1, 2, \ldots, N)$ and the microscale design variables $x_i^* \in [0, 1]$, $(i = 1, 2, \ldots, N)$ in each mesh element, respectively. For instance, $x_i^0 = x_i^* = 0$ represents that these elements are voids (the green regions in Fig. 4) and $x_i^0 = x_i^* = 1$ indicates that these elements are filled by material (the blue color regions in Fig. 4). Any intermediate
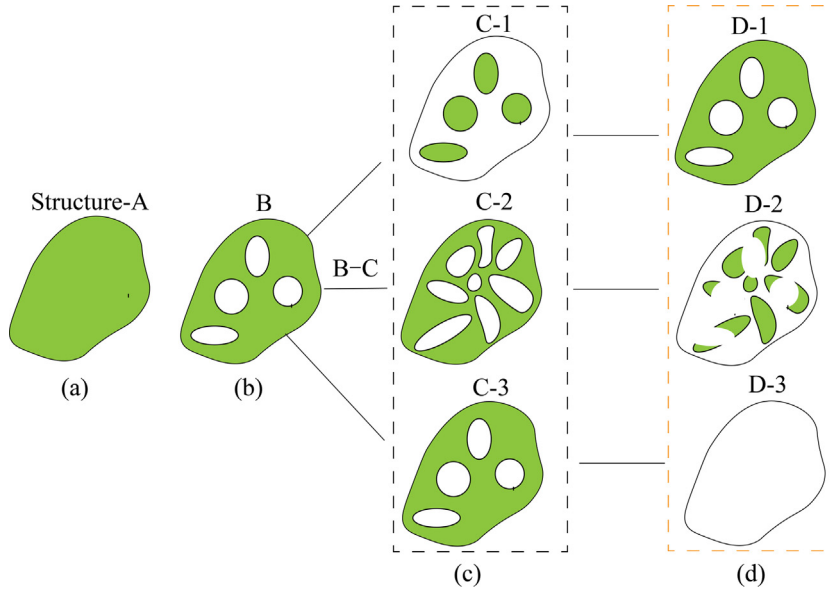
Fig. 3. Boolean subtraction operator: (a) reference structure A, (b) topology structure B, (c) three topology structures C1, C2 and C3, and (d) three topology structures D1, D2 and D3 obtained from the Boolean subtraction of structure-B and structures C1, C2 and C3. The corresponding subtraction operations are denoted as B–C1, B–C2, and B–C3, respectively.
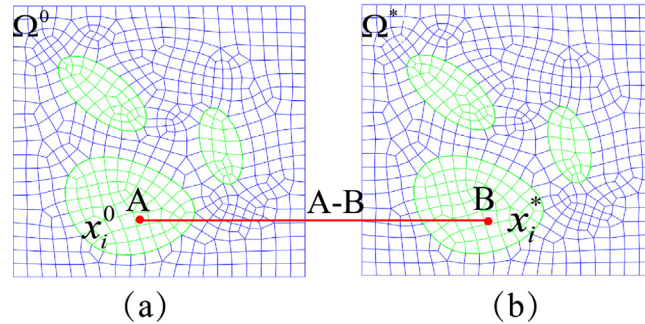
Fig. 4. Schematic illustration of the Boolean subtraction operator: (a) finite element meshes of the macrostructure, and (b) meshes of the microstructure. (For interpretation of the references to color in this figure legend, the reader is referred to the web version of this article.)

value in the range of (0, 1) indicates a false material element, referred to as the gray element problem. We use the SIMP method to solve this problem [28].

In terms of the design variables $x_i^0 \in [0, 1]$ and $x_i^* \in [0, 1]$, $(i = 1, 2, \ldots, N)$, the BSO of the structures in the two levels can be defined as

$$G_{\text{BSO}} = \frac{1}{N} \sum_{i=1}^{N} \left(x_i^0 - x_i^* \right)^2. \tag{1}$$

To ensure that points A and B in the macro- and micro-structures have the same phase (either void or solid), we can use the difference $x_i^0 - x_i^*$ to determine the result of 'A–B' between two element voxels, as shown in Fig. 4. For example, $x_i^0 - x_i^* = 0$ indicates that the voxel points A and B have the same material, while $x_i^0 - x_i^* \neq 0$ means that the material layout at A is different from that at B. Thus, Eq. (1) can translate the geometric description of BSO to the material value of voxel points. Mathematically, a hierarchical structure is regarded to be fractal or self-similar when its G_{BSO} value equals zero.

Besides the above-discussed gray element problem in the SIMP topology optimization model, the appearance of checkerboard patterns is another issue that needs to be solved [28,40]. Here, we use the density filtering method

to avoid the possibility for the occurrence of checkerboard patterns. In this method, the physical densities of the macroscale and microscale design variables are written as

$$\rho_i^0 = \frac{1}{\sum_{e \in N_i} H_{ie}^0} \sum_{e \in N_i} H_{ie}^0 x_e^0, \quad (i = 1, 2, \ldots, N), \tag{2}$$

$$\rho_i^* = \frac{1}{\sum_{e \in N_i} H_{ie}^*} \sum_{e \in N_i} H_{ie}^* x_e^*, \quad (i = 1, 2, \ldots, N), \tag{3}$$

respectively, where H_{ie} is the weight factor, and N_i is the set of elements whose center-to-center distance $\Delta(i, e)$ to the element e is smaller than the filter radius $r_{\min}$ [27,28]. Through this filtering process, the physical densities ρ_i^0 and ρ_i^* will be limited in the interval [0, 1]. Thus, Eq. (1) can be rewritten as

$$\tilde{G}_{BSO} = \frac{1}{N} \sum_{i=1}^{N} \left(\rho_{i,t}^0 - \rho_{i,t}^*\right)^2, \quad (i = 1, 2, \ldots, N). \tag{4}$$

In what follows, Eq. (4) will be used as an effective constraint in the topology optimization framework.

3. Concurrent topology optimization method

In this section, we will formulate a two-scale concurrent optimization framework for designing self-similar hierarchical structures. This framework can be easily extended to the design of higher-level structures. To control the material volume, we introduce the structural coverage constraint and the average porosity constraint, as in our previous work [33].

3.1. Topology optimization

In this study, we will take the maximum stiffness of the hierarchical structure subjected to uniaxial tension or compression as the objective function of optimization. Thus, the concurrent topology optimization problem can be formulated as the following mathematical programming problem:

$$\begin{aligned}
&\min_{\mathbf{x}^0, \mathbf{x}^*} : J = \mathbf{F}^{\mathrm{T}} \mathbf{U} \\
&\text{subject to} \quad : \mathbf{K}\left(\tilde{\mathbf{D}}, \mathbf{x}^0, \mathbf{x}^*\right) \mathbf{U} = \mathbf{F}, \\
&\quad : G_{SCC} = \sum_{k=1}^{N} \rho_k^0 s_k^0 - f_1 \left|\Omega^0\right| \le 0, \\
&\quad : G_{APC} = \sum_{k=1}^{N} \rho_k^0 s_k^0 \left(\frac{1}{N} \sum_{j=1}^{N} \rho_j^* s_j^*\right) - (1 - f_2) \sum_{k=1}^{N} \rho_k^0 s_k^0 \le 0, \\
&\quad : \tilde{G}_{BSO} = \sum_{k=1}^{N} \left(\rho_k^0 - \rho_k^*\right)^2 / N \le 0, \\
&\quad : 0 \le x_k^0, \ x_k^* \le 1, \ (k = 1, 2, \ldots, N),
\end{aligned} \tag{5}$$

where J, $\mathbf{K}$, and $\mathbf{F}$ denote the objective function, the global stiffness matrix, and the nodal force, respectively; $\mathbf{U}$ is the global nodal displacement vector in the macrostructure; functions G_{SCC} and G_{APC} correspond to the structural coverage constraint and the average porosity constraint, respectively; s_k^0 $(k = 1, 2, \ldots, N)$ and s_k^* $(k = 1, 2, \ldots, N)$ are the unit normalized element areas of the unit cells in the macrostructure and microstructure, respectively; $|\Omega_0|$ is the volume of the macrostructure, and f_1 and f_2 are the tuning weight factors in G_{SCC} and G_{APC}, respectively. The parameter G_{SCC} controls the layouts of microstructures, and G_{APC} restricts the total material volume. The effective elastic matrix $\tilde{\mathbf{D}}$ of the microstructure can be computed by solving the following microscopic elasticity equation in the weak form [35,36]:

$$\int_{\Omega^*} \left(\bar{\varepsilon}^*\right)^{\mathrm{T}} \mathbf{D}\bar{\varepsilon}(\delta) \, \mathrm{d}\,\Omega^* = \int_{\Omega^*} \left(\bar{\varepsilon}^0\right)^{\mathrm{T}} \mathbf{D}\bar{\varepsilon}(\delta) \, \mathrm{d}\,\Omega^*, \tag{6}$$

where $\bar{\boldsymbol{\varepsilon}}^* = \mathbf{B}\boldsymbol{\chi}^*$ and $\bar{\boldsymbol{\varepsilon}}^0$ denote the characteristic strain tensor and the unit test strain tensor in the unit cell, $\boldsymbol{\delta}$ is $|\Omega^*|$-periodic virtual displacement field in the microstructure, $\mathbf{B}$ and $\boldsymbol{\chi}^*$ are the strain–displacement matrix and the characteristic displacement field, respectively. $\mathbf{D}$ is the material elastic matrix at the micro level and can be written as

$$\mathbf{D} = \left[E_{\min} + \left(\rho^* \right)^p E_{\mathrm{s}} \right] \mathbf{D}_0, \tag{7}$$

where $E_{\min}$ and E_{S} are an infinitesimal positive number and the Young's modulus of the based material, respectively, $\mathbf{D}_0$ is the elastic matrix of the based material, and P is the penalty factor. For 2D problems, we chose three unit test strain fields $\bar{\boldsymbol{\varepsilon}}^0 = [1, 0, 0]^{\mathrm{T}}$, $[0, 1, 0]^{\mathrm{T}}$ and $[0, 0, 1]^{\mathrm{T}}$; whereas for 3D problems, we chose six unit strain fields $\bar{\boldsymbol{\varepsilon}}^0 = [1, 0, 0, 0, 0, 0]^{\mathrm{T}}$, $[0, 1, 0, 0, 0, 0]^{\mathrm{T}}$, $[0, 0, 1, 0, 0, 0]^{\mathrm{T}}$, $[0, 0, 0, 1, 0, 0]^{\mathrm{T}}$, $[0, 0, 0, 0, 1, 0]^{\mathrm{T}}$ and $[0, 0, 0, 0, 0, 1]^{\mathrm{T}}$ on the microstructure under periodic boundary conditions. Then the effective elastic matrix can be computed by [35,36,41]

$$\tilde{\mathbf{D}} = \frac{1}{|\Omega^*|} \int_{\Omega^*} \left(\boldsymbol{\varepsilon}^* - \boldsymbol{\varepsilon}^0 \right)^{\mathrm{T}} \mathbf{D} \left(\boldsymbol{\varepsilon}^* - \boldsymbol{\varepsilon}^0 \right) \mathrm{d}\,\Omega^*, \tag{8}$$

where $|\Omega^*|$ is the volume of the microstructure. In the present concurrent method, the elastic matrix of the kth macro-element can be written as

$$\mathbf{D}_k^{\mathrm{M}} = \mathbf{D}_{\min} + \left(\rho_k^0 \right)^{\eta} \tilde{\mathbf{D}}, \quad (k = 1, 2, \ldots, N) . \tag{9}$$

For the simplicity of formulation, we assume that the macrostructure has only one type of unit cells, though the present framework can be easily extended to structures consisting of different unit cells.

3.2. Sensitivity analysis with respect to macroscale design variables

To solve the optimization problem defined in Eq. (5), we employ the method of moving asymptote (MMA) [42], which has a gradient operator, to update all macroscale and microscale design variables. In MMA, the gradient information and the sensitivity information of objective functions and constraints need to be provided in terms of the design variables in both levels of structures. Because the maximum stiffness problem in Eq. (5) has the self-adjoint property [27,28], and the sensitivity of the objective function can be easily written in terms of the macroscale design variables as

$$\frac{\partial J \left(\mathbf{x}^0, \mathbf{x}^* \right)}{\partial x_i^0} = -\sum_{k=1}^{N} \mathbf{u}_k^{\mathrm{T}} \frac{\partial \mathbf{k}_k}{\partial x_i^0} \mathbf{u}_k = -\sum_{k=1}^{N} \mathbf{u}_k^{\mathrm{T}} \left(\int_{\Omega_k^0} \mathbf{B}^{\mathrm{T}} \frac{\partial \mathbf{D}_k^{\mathrm{M}}}{\partial x_i^0} \mathbf{B} \, \mathrm{d}\, \Omega_k^0 \right) \mathbf{u}_k \tag{10}$$

$$= -\sum_{k=1}^{N} \mathbf{u}_k^{\mathrm{T}} \left[\eta \left(\rho_k^0 \right)^{(\eta-1)} \frac{\partial \rho_k^0}{\partial x_i^0} \int_{\Omega_k^0} \mathbf{B}^{\mathrm{T}} \tilde{\mathbf{D}} \mathbf{B} \mathrm{d}\, \Omega_k^0 \right] \mathbf{u}_k, \quad (i = 1, 2, \ldots, N) .$$

Similarly, the derivatives of structural coverage constraint G_{SCC}, the structural porosity constraint G_{APC}, and the Boolean subtraction constraint $\tilde{G}_{\mathrm{BSO}}$ with respect to the macroscale design variables are calculated by

$$\frac{\partial G_{\mathrm{SCC}}}{\partial x_i^0} = \sum_{k=1}^{N} \frac{\partial \rho_k^0}{\partial x_i^0} s_k^0, \quad (i = 1, 2, \ldots, N) , \tag{11}$$

$$\frac{\partial G_{\mathrm{APC}}}{\partial x_i^0} = \sum_{k=1}^{N} \frac{\partial \rho_k^0}{\partial x_i^0} s_k^0 \left[\frac{1}{N} \sum_{j}^{N} \rho_j^* s_j^* - (1 - f_2) \right], \quad (i = 1, 2, \ldots, N) , \tag{12}$$

$$\frac{\partial \tilde{G}_{\mathrm{BSO}}}{\partial x_i^0} = \sum_{k=1}^{N} \frac{2 \left(\rho_k^0 - \rho_k^* \right)}{N} \frac{\partial \rho_k^0}{\partial x_i^0}, \quad (i = 1, 2, \ldots, N) , \tag{13}$$

where the indexes k obey the Einstein's summation convention. The derivative of $\partial \rho_k^0 / \partial x_i^0$ can be computed easily from Eq. (2).

3.3. Sensitivity analysis with respect to microscale design variables

Analogously to Section 3.2, the sensitivity of the objective function with respect to the microscale design variables is determined by

$$
\frac{\partial J\left(\mathbf{x}^{0}, \mathbf{x}^{*}\right)}{\partial x_{i}^{*}} = -\sum_{k}^{N} \mathbf{u}_{k}^{\mathrm{T}} \int_{\mathbf{\Omega}_{k}^{*}} \mathbf{B}^{\mathrm{T}} \frac{\partial \mathbf{D}_{k}^{\mathrm{M}}}{\partial x_{i}^{*}} \mathbf{B} \, \mathrm{d}\, \Omega_{k}^{*} \mathbf{u}_{k} \tag{14}
$$

$$
= -\sum_{k}^{N} \mathbf{u}_{k}^{\mathrm{T}} \int_{\mathbf{\Omega}_{k}^{*}} \mathbf{B}^{\mathrm{T}} \left[\left(\rho_{k}^{0}\right)^{\eta} \frac{\partial \tilde{\mathbf{D}}}{\partial x_{i}^{*}} \right] \mathbf{B} \, \mathrm{d}\, \Omega_{k}^{*} \mathbf{u}_{k}, \quad (i = 1, 2, \ldots, N).
$$

Here, the derivative of $\tilde{\mathbf{D}}$ can be obtained as

$$
\frac{\partial \tilde{\mathbf{D}}}{\partial x_{i}^{*}} = \sum_{k=1}^{N} \frac{p\left(\rho_{k}^{*}\right)^{(p-1)} E_{\mathrm{s}}}{|\Omega^{*}|} \frac{\partial \rho_{k}^{*}}{\partial x_{i}^{*}} \int_{\Omega^{*}} \left(\boldsymbol{\varepsilon}^{*} - \boldsymbol{\varepsilon}^{0}\right)^{\mathrm{T}} \mathbf{D}_{0} \left(\boldsymbol{\varepsilon}^{*} - \boldsymbol{\varepsilon}^{0}\right) \mathrm{d}\, \Omega^{*}, \quad (i = 1, 2, \ldots, N), \tag{15}
$$

where the derivative $\partial \rho_{k}^{*} / \partial x_{i}^{*}$ can be computed easily from Eq. (3).

The derivatives of the structural coverage constraint G_{SCC}, the structural porosity constraint G_{APC}, and the Boolean subtraction constraint $\tilde{G}_{\mathrm{BSO}}$ with respect to the microscale design variables are written as

$$
\frac{\partial G_{\mathrm{SCC}}}{\partial x_{i}^{0}} = 0, \quad (i = 1, 2, \ldots, N), \tag{16}
$$

$$
\frac{\partial G_{\mathrm{APC}}}{\partial x_{i}^{*}} = \sum_{k=1}^{N} \rho_{k}^{0} s_{k}^{0} \left(\frac{1}{N} \sum_{j=1}^{N} \frac{\partial \rho_{j}^{*}}{\partial x_{i}^{*}} s_{j}^{*} \right) - (1 - f_{2}) \sum_{i=1}^{N} \rho_{k}^{0} s_{k}^{0}, \quad (i = 1, 2, \ldots, N), \tag{17}
$$

$$
\frac{\partial \tilde{G}_{\mathrm{BSO}}}{\partial x_{i}^{0}} = -\sum_{k=1}^{N} \frac{2 \left(\rho_{k}^{0} - \rho_{k}^{*}\right)}{N} \frac{\partial \rho_{k}^{*}}{\partial x_{i}^{0}}, \quad (i = 1, 2, \ldots, N). \tag{18}
$$

All sensitivity information can be solved from Eqs. (9)–(18). Then the optimization iteration process will be terminated when the maximum error of all design variables between the two adjacent iteration steps become less than 0.0001 or the maximum iteration number reaches up to 200.

4. Examples and discussions

The above topology optimization method based on the Boolean subtraction operator allows us to design materials with both 2D and 3D hierarchical structures. In this section, we provide a few examples of 2D square structures and 3D cubic structures to illustrate the application of this method. In all 2D examples, both the macrostructure and microstructure have $nx \times ny$ four-node bilinear square elements, as shown in Fig. 3(a), while all 3D structures have $nx \times ny \times nz$ eight-node bilinear cubic elements, as shown in Fig. 3(b). We set $nx \times ny = 60$ for the 2D problems, and $nx \times ny \times nz = 40$ for the 3D problems. The elements are numbered following the order from the upper to the bottom, from the left to the right, and from the back to the front, as shown the 2D in Fig. 5(a) and 3D in Fig. 5(b). The boundary conditions and nodal loads we have specified in the calculations are also given in Fig. 5. The dimensionless Young's modulus and Poisson's ratio of the based material in the microstructure are set to be 10 and 0.3, respectively. All examples are performed through a MATLAB program.

4.1. Verification of the Boolean subtraction operator

The concurrent topology optimization formulated in Section 2 is first used to design hinged-end planar structures. Two examples are given below, with the boundary conditions and nodal loads being listed in Table A.1 (Appendix). The first structure is designed under the Boolean subtraction constraint (Fig. 6a), while the other is not (Fig. 6b). The tunable parameters in Eq. (5) are set as $f_{1} = 0.5$ and $f_{2} = 0.5$. The optimized results are shown in Fig. 6(a) and (b) with the objective function values $J = 18.4$ and $J = 22.0$, respectively. Without implementing the Boolean
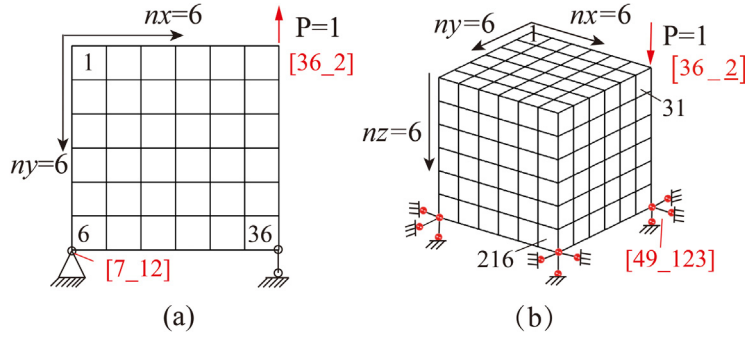
Fig. 5. The element numbers (black color) and node numbers (red color) in (a) the 2D and (b) 3D structures. (For interpretation of the references to color in this figure legend, the reader is referred to the web version of this article.)
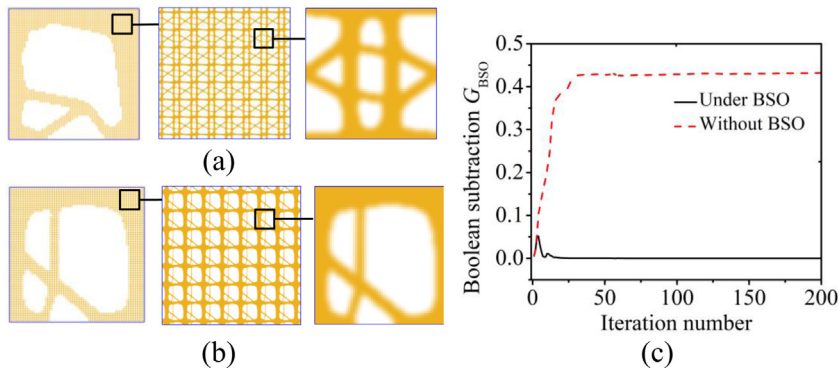
Fig. 6. Verification of the Boolean subtraction constraint: (a) the optimized fractal structure using the Boolean subtraction constraint, (b) the optimized structure without the Boolean subtraction constraint, (c) the iteration history of the Boolean subtraction constraint.

subtraction constraint into the optimization scheme, the topology in the microstructure in Fig. 6(a) is not like that in the macrostructure, while the result shown in Fig. 6(b) has the same morphological shape at both microscale and macroscale levels. This is because that under the Boolean constraint, the difference of the material layouts in the macrostructure and microstructure can gradually reduce to zero. When $\tilde{G}_{BSO}$ gets to be zero, the macrostructure and microstructure will have the same topology. However, the results in Fig. 6(a) without introducing the Boolean subtraction constraint have a large value of $\tilde{G}_{BSO}$ even after many optimization iterations [Fig. 6(c)]. Besides, from the iteration history curve in Fig. 6(c), the present optimization method converges quickly within 50 steps and the whole optimization process is very stable. Therefore, the proposed method shows a high efficiency and robustness in the design of fractal structures.

4.2. Multi-load design of fractal structures

For the structure in Fig. 6(a), despite the self-similarity of micro- and macro-structures, it is still difficult to obtain a symmetric or chiral hierarchical structure because of the single boundary and loading conditions assumed in Section 4.1. To design structures with symmetric or chiral features, we further improve the above scheme. To this end, we apply four different loads and boundary conditions on the macrostructure and rewrite the assembling objective function as

$$J\left(\mathbf{x}^0, \mathbf{x}^*\right) = \sum_{l=1}^{L} \mathbf{F}_l^{\mathrm{T}} \mathbf{U}_l, \tag{19}$$

where L is the total number of loading situations we consider in the optimization. It is noted that, for the multi-load case, the number of the design variables remains unchanged. In the 2D example, L is set to be 4 and the details
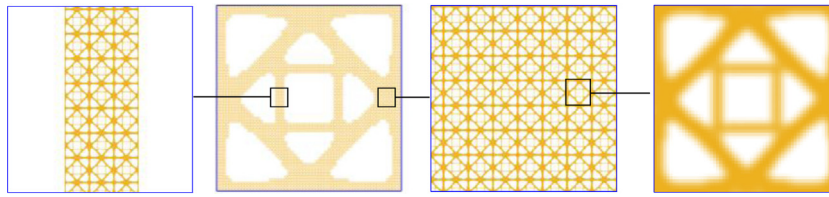
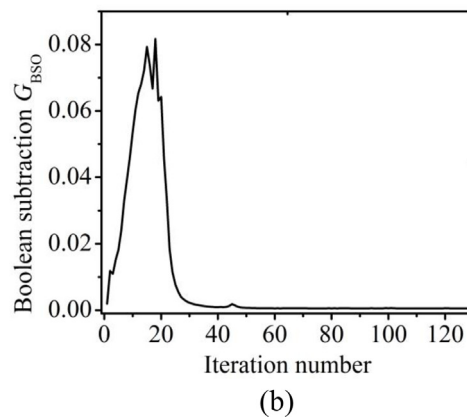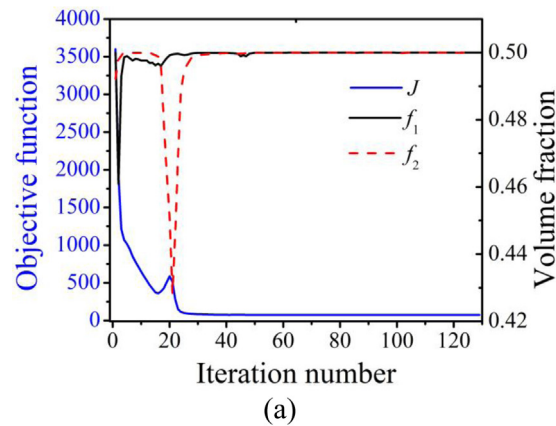**Fig. 7.** Optimized fractal hierarchical structure under multi-load condition.

Fig. 8. Iteration history curves of (a) the objective function and material volume fraction, and (b) Boolean subtraction constraint factor.

of the four loads and boundary conditions we assume in the calculation are listed in Table A.1 (Appendix). In this example, we first consider four symmetric loads and boundary conditions. The obtained fractal structure with the objective function value $J = 78.5$ is given in Fig. 7, in which the microstructure has the identical morphology as the macrostructure, and both the macro- and micro-structures have the mirror symmetry property along all directions of the x, y, and diagonal axes. The iteration history curves of the objective function, the material volume fraction, and the Boolean subtraction constraint factor are given in Fig. 8. This example demonstrates that this enhanced method can be used to design structures with specific symmetry or chirality through the consideration of multi-load cases, rather than a single load mode.

To design hierarchical structures with chiral morphology, we specify two different twisting loads and four boundary conditions, as shown in Fig. 6. The details of loading and boundary conditions are listed in Table A.1 (Appendix). Thus, we obtain two chiral fractal structures with the objective function values $J = 47.14$ and $J = 118.7$, as shown in Fig. 9. Here the chirality of a structure is defined by the rotating orientation from a
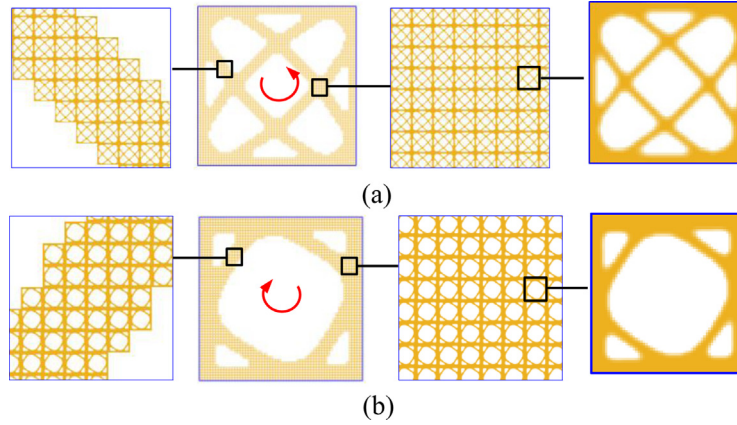
(a)

(b)

Fig. 9. Fractal structures with (a) weak counterclockwise and (b) clockwise chirality.

symmetric axis of the square region to the corresponding axis of its structure. The optimized structure in Fig. 9(a) has the feature of weak chiral, counterclockwise morphology while that in Fig. 9(b) is clockwise. The macro- and micro-structures have the same chiral topology except their difference in the characteristic sizes. By adjusting the twisting loads, we can obtain fractal structures with weak (Fig. 9a) and strong (Fig. 9b) chirality. If the applied twisting loads are reversed in direction, the chirality of the optimized structures can also be reversed. Therefore, the present concurrent topology scheme enables to design hierarchical structures with different chirality through the application of external torques in the simulations.

4.3. Three-dimension fractal structures

In contrast to the 2D structures illustrated in Section 4.2, 3D structures have three directions of voxel layouts. To ensure the stability of the optimization process, we introduce the 3D Boolean subtraction constraint, which is expressed as

$$\tilde{G}_{\text{BSO}} \equiv \frac{1}{N} \sum_{k=1}^{N} \left[\left(1 - \rho_k^0\right)^2 - \left(1 - \rho_k^*\right)^2 \right]^2 \leq 0. \tag{20}$$

A few representative examples will be given below to demonstrate the application of the presented method for designing 3D hierarchical structures.

In the first example, we set the parameters $f_1 = 0.2$ and $f_2 = 0.8$. The six symmetric loading and boundary conditions we specify are given in Table A.2 (Appendix). To more clearly show the optimized 3D structure, we plot the isosurface with the optimized design variables larger than 0.5. The optimized macrostructure in Fig. 10(a) with the objective function value $J = 7.84$ has the same topology as the microstructure shown in Fig. 10(b). Though this structure resembles the classical face centered cubic (FCC) lattice structure consisting of straight bars obtained in the previous studies [23,24], the internal struts shown in Fig. 10(b) are slightly curved. This example proves that the topology optimization method proposed in this work can efficiently yield various 3D fractal structures by controlling the loading and boundary conditions.

In the second example, we set the parameters $f_1 = 0.3$ and $f_2 = 0.7$. Four symmetric loading and boundary conditions are applied on the nodal points at the right, left, front, and back surfaces (Table A.2 in the Appendix). The optimized fractal macro- and micro-structures with the objective function value $J = 4.01$ are shown in Fig. 11(a) and (b), respectively. The two levels of structures have the same morphology consisting of shell or bent plate elements. It is well known that, when subjected to some special loads, the structures consisting of shell and plate elements have better mechanical properties than lattice structures consisting of bars [43–46].

The material volume fraction is a key parameter that significantly influences the mechanical properties of the designed structure. To examine this aspect, we change the values of f_1 and f_2, as listed in Table 1. We find that some voids will emerge in the bent shell structures as the value of f_1 approaches 0.2. This is because that the finite element
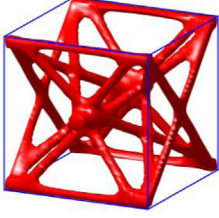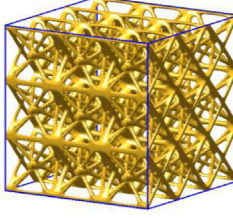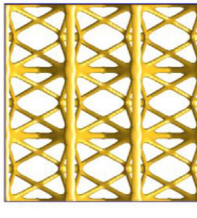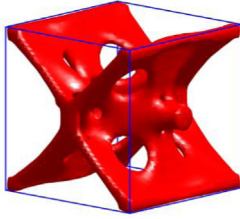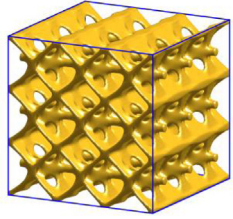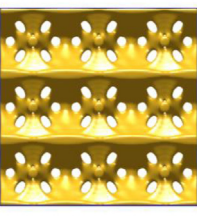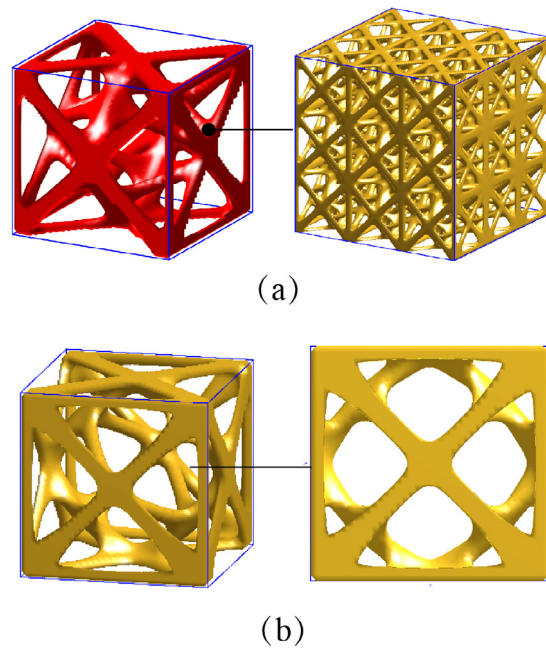
Fig. 10. (a) Macrostructure and (b) microstructure in the designed 3D fractal structure.
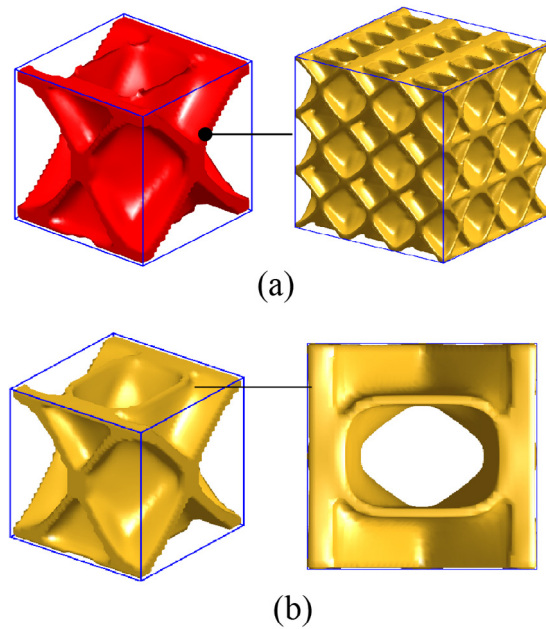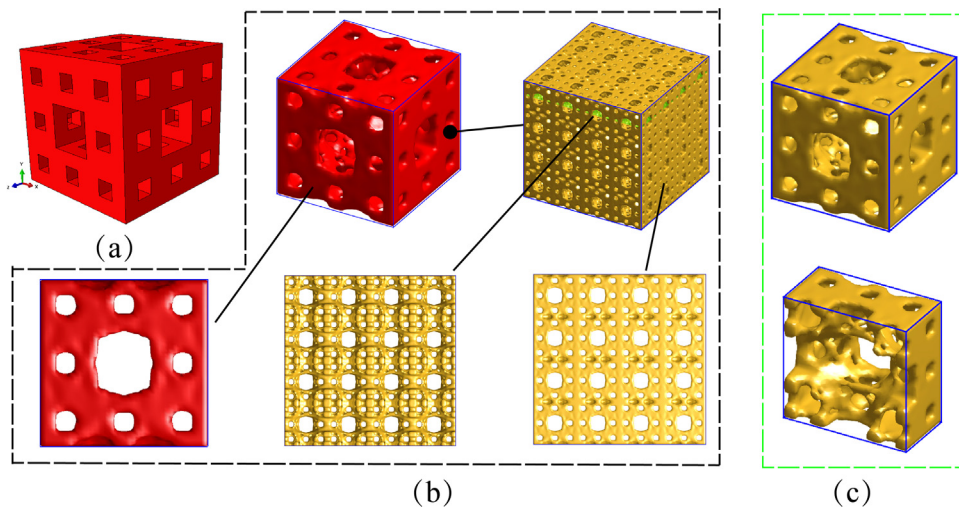
Fig. 11. (a) Macrostructure and (b) microstructure in the optimized 3D fractal structures consisting of shell and bent plate elements.

numbers in the macro- and micro-structures are finite ($40 \times 40 \times 40$), and the formation voids in the perfect shell structures can further lower the material volume fraction [47]. When f_1 decreases to a small number (e.g., 0.1), the fractal structure will transform from a shell topology to a lattice, as shown in Table 1. Corresponding to the decrease in the material volume fraction, the effective stiffness of the obtained fractal structure decreases remarkably. Such a transformation from shell structures to lattice structures is close to the structural evolution of bone with aging, especially under the pathological conditions of osteoporosis. The application of the present topology optimization

Table 1
Effects of parameters f_1 and f_2.

|	macrostructure	microstructure	side view
$f_1 = 0.1$ $f_2 = 0.9$ $J = 45.64$			
$f_1 = 0.2$ $f_2 = 0.8$ $J = 5.90$			

Fig. 12. Optimized 3D hybrid fractal structure with the feature of Menger sponge: (a) Menger sponge structure, (b) the optimized fractal structure, and (c) the microstructure and its half showing the internal morphology.

method to such biological materials as bone holds promise for important application in medical engineering and will be further studied in our next work.

4.4. Menger sponge

The Menger sponge is a classical fractal graph, but it remains unclear how to design such super-structures from the viewpoint of mechanical principle. To further illustrate the diverse application of the present topology method, we will design this kind of structures following a straightforward routine. Unlike the above examples, we here introduce a fractal Menger sponge as the designed domain (the solid material regions), as shown in Fig. 12(a). For example, we set the parameters $f_1 = 0.3$ and $f_2 = 0.7$. Six symmetric loading and boundary conditions are applied

(a)

(b)

(c)
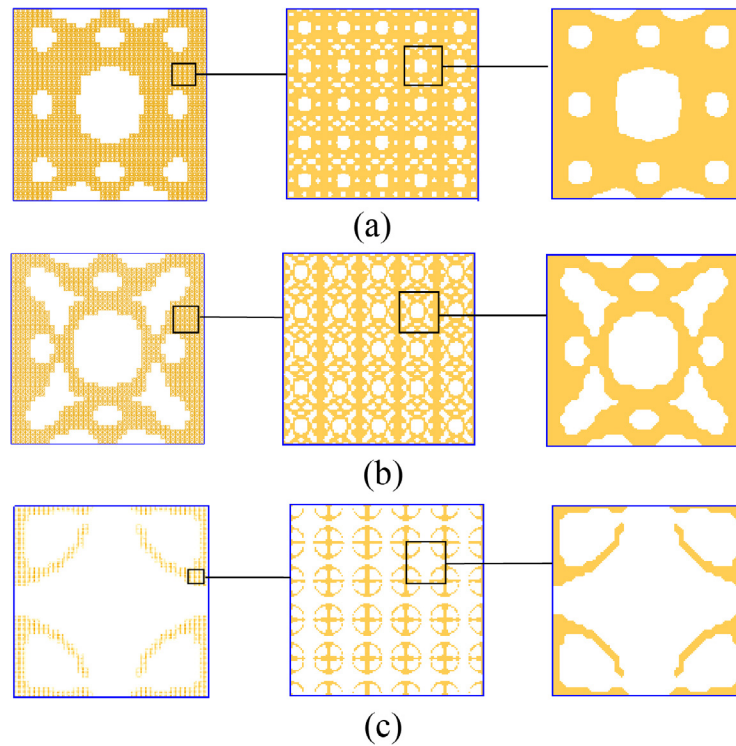
Fig. 13. Three representative cross-sections of the optimized 3D fractal structure shown in Fig. 12(b).

Table A.1

The fixed nodal freedoms and nodal loads in different 2D examples.

Cases	Fixed nodal freedoms	Loads
Fig. 6	$[2\,(ny+1)\,\_12]$, $[2\,(ny+1)\,(nx+1)\,\_1]$.	$[1\_12]$, $[(ny+1)\,nx+1\_12]$.
Fig. 7	$[2\,(ny+1)\,\_12]$, $[(ny+1)\,(nx+1)\,\_1]$;	$[(ny+1)\,nx/2+1\_2]$; $[(ny+1)\,nx+ny/2+1\_1]$; $[(ny+1)\,(nx/2+1)\,\_2]$; $[ny/2+1\_1]$.
Fig. 9(a)	$[1\_12]$, $[(ny+1)\,\_1]$; $[1\_2]$, $[(ny+1)\,nx+1\_12]$; $[(ny+1)\,nx\_1]$, $[(ny+1)\,(nx+1)\,\_12]$.	$[10\,(ny+1)+1\_1]$; $[(ny+1)\,nx+11\_2]$; $[(ny+1)\,(nx-9)\,\_1]$; $[ny-9\_2]$.
Fig. 9(b)		$[(ny+1)\,nx/2+1\_1]$, $[(ny+1)\,nx+1\_2]$; $[(ny+1)\,nx+ny/2+1\_2]$, $[(ny+1)\,(nx+1)\,\_1]$; $[(ny+1)\,(nx/2+1)\,\_1]$, $[(ny+1)\,\_2]$; $[ny/2+1\_2]$, $[1\_1]$.

on the specified nodes at the six surfaces in the optimization domain (see Table A.2 in the Appendix for details). Through the topology optimization scheme, the obtained macrostructure with the objective function value $J = 7.84$ and the corresponding microstructure are given in Fig. 12(b) and (c), respectively. It is clear that all surfaces of the optimized fractal structure exhibit the geometric characteristics of Menger sponge at both levels.

To more clearly illustrate the complex internal topologies in Fig. 12, three representative cross-sections of the optimized self-similar structure in Fig. 12(b) are given in Fig. 13(a–c), which all have fractal patterns at the macro and micro levels. It is emphasized that, besides the Menger sponge, some other fractal graphs can also be employed analogously to construct novel hierarchical structures.

Table A.2
The fixed nodal freedoms and nodal loads in the 3D examples.

Cases	Fixed nodal freedoms	Loads
Fig. 10	$[1\_123]$, $[(ny+1)\_123]$, $[(ny+1)(nx+1)nz+ny+1\_123]$, $[(ny+1)(nx+1)nz+1\_123]$; $[1\_123]$, $[(ny+1)\_123]$, $[(ny+1)nx+1\_123]$, $[(ny+1)(nx+1)\_123]$; $[(ny+1)nx+1\_123]$, $[(ny+1)(nx+1)\_123]$, $[(ny+1)(nx+1)nz+(ny+1)nx+1\_123]$, $(ny+1)(nx+1)nz+(ny+1)(nx+1)$; $(ny+1)(nx+1)nz+1\_123$, $[(ny+1)(nx+1)nz+(ny+1)\_123]$, $[(ny+1)(nx+1)nz+(ny+1)nx+1\_123]$, $[(ny+1)(nx+1)nz+(ny+1)(nx+1)\_123]$; $[1\_123]$, $[(ny+1)nx+1\_123]$, $[(ny+1)(nx+1)nz+1\_123]$, $[(ny+1)(nx+1)nz+(ny+1)nx+1\_123]$; $[(ny+1)\_123]$, $[(ny+1)(nx+1)\_123]$, $[(ny+1)(nx+1)nx+(ny+1)\_123]$, $[(ny+1)(nx+1)(nz+1)\_123]$.	$\begin{bmatrix}(ny+1)(nx+1)nz/2+\\(ny+1)nx/2+ny/2\_1\end{bmatrix}$; $\begin{bmatrix}(ny+1)(nx+1)nz+\\(ny+1)nx/2+ny/2+1\_3\end{bmatrix}$; $[(ny+1)(nx+1)nz/2+ny/2+1\_\underline{1}]$; $[(ny+1)nx/2+ny/2+1\_\underline{3}]$; $\begin{bmatrix}(ny+1)(nx+1)nz/2+\\(ny+1)nz/2+1\_2\end{bmatrix}$; $\begin{bmatrix}(ny+1)(nx+1)nz/2+\\(ny+1)(nx/2+1)\_2\end{bmatrix}$.
Fig. 11	$[1\_123]$, $[(ny+1)\_123]$, $[(ny+1)(nx+1)nz+ny+1\_123]$, $[(ny+1)(nx+1)nz+1\_123]$; $[1\_123]$, $[(ny+1)\_123]$, $[(ny+1)nx+1\_123]$, $[(ny+1)(nx+1)\_123]$; $[(ny+1)nx+1\_123]$, $[(ny+1)(nx+1)\_123]$, $[(ny+1)(nx+1)nz+(ny+1)nx+1\_123]$, $[(ny+1)(nx+1)nz+(ny+1)(nx+1)]$; $[(ny+1)(nx+1)nz+1\_123]$, $[(ny+1)(nx+1)nz+(ny+1)\_123]$, $[(ny+1)(nx+1)nz+(ny+1)nx+1\_123]$, $[(ny+1)(nx+1)nz+(ny+1)(nx+1)\_123]$;	$\begin{bmatrix}(ny+1)(nx+1)nz/2+\\(ny+1)nx/2+ny/2\_1\end{bmatrix}$; $\begin{bmatrix}(ny+1)(nx+1)nz+\\(ny+1)nx/2+ny/2+1\_3\end{bmatrix}$; $[(ny+1)(nx+1)nz/2+ny/2+1\_\underline{1}]$; $\begin{bmatrix}(ny+1)nx/2+ny/2+1\_\underline{3}\end{bmatrix}$.

5. Conclusions

In summary, we have proposed a concurrent topology optimization method by introducing the Boolean subtraction operator (BSO) to design both 2D and 3D fractal structures. The BSO functions to guarantee the geometric similarity between the macro- and micro-structures. By specifying multiple loads, the presented method allows us to design chiral fractal structures with required symmetric or chiral morphologies. The clockwise and counterclockwise properties of 2D structures can be realized by the application of twisting loading conditions. A few 2D and 3D fractal structures have been given as examples to demonstrate the efficiency and robustness of the proposed scheme. Different types of hierarchical structures consisting of plate and shell elements can be obtained with superior mechanical properties. In addition, such fractal graphs as the Menger sponge can also be invoked to construct hierarchical structures with particular topological characteristics.

The examples shown in Section 4 demonstrate that the proposed topology optimization method is simple, efficient, and robust in the design of materials with fractal structures. Though we address mainly the mechanical properties of materials in this paper, the proposed method can also be extended to design 2D and 3D fractal structures with novel optical, acoustic, and electromagnetic properties. In these cases, the mathematical programming problem in Section 3.1 should be modified by introducing the corresponding structure–function relationship. Finally, it is worth mentioning that the assumptions of linear constitutive relation and small deformation have been made in this

Table A.2 (*continued*).

Cases	Fixed nodal freedoms	Loads
Fig. 12	$[1\_123]$, $[(ny+1)\_123]$, $[(ny+1)(nx+1)nz+ny+1\_123]$, $[(ny+1)(nx+1)nz+1\_123]$; $[1\_123]$, $[(ny+1)\_123]$, $[(ny+1)nx+1\_123]$, $[(ny+1)(nx+1)\_123]$; $[(ny+1)nx+1\_123]$, $[(ny+1)(nx+1)\_123]$, $[(ny+1)(nx+1)nz+(ny+1)nx+1\_123]$, $[(ny+1)(nx+1)nz+(ny+1)(nx+1)]$; $[(ny+1)(nx+1)nz+1\_123]$, $[(ny+1)(nx+1)nz+(ny+1)\_123]$, $[(ny+1)(nx+1)nz+(ny+1)nx+1\_123]$, $[(ny+1)(nx+1)nz+(ny+1)(nx+1)\_123]$; $[1\_123]$, $[(ny+1)nx+1\_123]$, $[(ny+1)(nx+1)nz+1\_123]$, $[(ny+1)(nx+1)nz+(ny+1)nx+1\_123]$; $[(ny+1)\_123]$, $[(ny+1)(nx+1)\_123]$, $[(ny+1)(nx+1)nx+(ny+1)\_123]$, $[(ny+1)(nx+1)(nz+1)\_123]$.	$[14(ny+1)(nx+1)+(ny+1)nx+15\_1]$, $[14(ny+1)(nx+1)+(ny+1)nx+27\_1]$, $[26(ny+1)(nx+1)+(ny+1)nx+15\_1]$, $[26(ny+1)(nx+1)+(ny+1)nx+27\_1]$; $[(ny+1)(nx+1)nz+14(ny+1)+15\_3]$, $[(ny+1)(nx+1)nz+26(ny+1)+15\_3]$, $[(ny+1)(nx+1)nz+14(ny+1)+27\_3]$, $[(ny+1)(nx+1)nz+26(ny+1)+27\_3]$; $[14(ny+1)(nx+1)+15\_\underline{1}]$, $[14(ny+1)(nx+1)+27\_\underline{1}]$, $[26(ny+1)(nx+1)+15\_\underline{1}]$, $[26(ny+1)(nx+1)+27\_\underline{1}]$; $\left[14(ny+1)+15\_\underline{3}\right]$, $\left[26(ny+1)+15\_\underline{3}\right]$, $\left[14(ny+1)+27\_\underline{3}\right]$, $\left[26(ny+1)+27\_\underline{3}\right]$; $[14(ny+1)(nx+1)+14(ny+1)+1\_2]$, $[26(ny+1)(nx+1)+14(ny+1)+1\_2]$, $14(ny+1)(nx+1)+26(ny+1)+1\_2[]$, $[26(ny+1)(nx+1)+26(ny+1)+1\_2]$; $[14(ny+1)(nx+1)+15(ny+1)\_2]$, $[26(ny+1)(nx+1)+15(ny+1)\_2]$, $[14(ny+1)(nx+1)+27(ny+1)\_2]$, $[26(ny+1)(nx+1)+27(ny+1)\_\underline{2}]$.

work, this method deserves to be extended to flexible structures and devices comprising superelastic soft materials subject to large deformations

Declaration of competing interest

The authors declare that they have no known competing financial interests or personal relationships that could have appeared to influence the work reported in this paper.

Acknowledgments

Appendix

In this appendix, we introduce the symbols [index_12] and [index_123] to represent the fixed nodal freedoms of 2D and 3D (Fig. 5) structural boundary conditions (the second column in Table A.1). For example, [20_123] means that the *x*, *y* and *z*-direction freedoms of the 20th node are fixed, and the [10_13] means that the opposite *x* and *z*-direction freedoms are applied with unit loads (the third column in Table A.1). The semicolon symbol ';' in the table distinguishes the different groups of loading and boundary conditions.

References

[1] B. Mandelbrot, How long is the coast of Britain? Statistical self-similarity and fractional dimension, Science 156 (1967) 636–638.

[2] T. Matsuyama, M. Mstsushita, Fractal morphogenesis by a bacterial cell population, Critical Rev. Microbiol. 19 (1993) 117–135.

[3] L.A. Di, F. Grizzi, H. Jelinek, A.J. Pellionisz, G.A. Losa, Fractals in the neurosciences, part i: general principles and basic neurosciences, Neuroscientist 20 (2014) 403–417.

[4] P. Waliszewski, F. Wagenlehner, S. Gattenlöhner, On the relationship between tumor structure and complexity of the spatial distribution of cancer cell nuclei: a fractal geometrical model of prostate carcinoma, Prostate 75 (2015) 399–414.

[5] M.V. Nichita, M.A. Paun, V.A. Paun, V.P. Paun, Fractal analysis of brain glial cells, Fract. Dimens. Lacunarity, Univ. Politeh. Buchar. Sci. Bull.-Ser. A-Appl. Math. Phys. 81 (2019) 273–284.

[6] C.M. Rosetti, B. Maggio, Protein-induced surface structuring in myelin membrane monolayers, Biophys. J. 93 (2007) 4254–4267.

[7] T. Wischgoll, J. Meyer, B. Kaimovitz, Y. Lanir, G.S. Kassab, A novel method for visualization of entire coronary arterial tree, Ann. Biomed. Eng. 35 (2007) 694–710.

[8] H.Y. Guo, Q.Y. Li, H.P. Zhao, K. Zhou, X.Q. Feng, Functional map of biological and biomemetic materials with hierarchical surface structures, RSC Adv. 5 (2015) 66901–66926.

[9] S.H. Ngoc, G.X. Lu, A review of recent research on bio-inspired structures and materials for energy absorption applications, Composites B (2019) 107496.

[10] J. Wang, Y. Zhang, N. He, H.C. Wang, Crashworthiness behavior of koch fractal structures, Mater. Des. 144 (2018) 229–244.

[11] Y. Zhang, J. Wang, C. Wang, Y. Zeng, T. Chen, Crashworthiness of bionic fractal hierarchical structures, Mater. Des. 158 (2018) 147–159.

[12] A.S. Fallah, N. Navadeh, V.V. Tereshchuk, V.N. Gorshkov, Phononic dispersion in anisotropic pseudo-fractal hyper-lattices, Mater. Des. 164 (2019) 107560.

[13] V. Kunin, S. Yang, Y. Cho, P. Deymier, D.J. Srolovitz, Static and dynamic elastic properties of fractal-cut materials, Extreme Mech. Lett. 6 (2016) 103–114.

[14] J. Liu, L. Li, B.Z. Xia, X.F. Man, Fractal labyrinthine acoustic metamaterial in planar lattices, Int. J. Solids Struct. 132 (2018) 20–30.

[15] X.F. Man, T. Liu, B.Z. Xia, Z. Luo, L. Xie, J. Liu, Space-coiling fractal metamaterial with multi-bandgaps on subwavelength scale, J. Sound Vib. 423 (2018) 322–339.

[16] X.F. Man, Z. Luo, J. Liu, B.Z. Xia, Hilbert fractal acoustic metamaterials with negative mass density and bulk modulus on subwavelength scale, Mater. Des. 180 (2019) 107911.

[17] G. Pia, E. Sassoni, E. Franzoni, U. Sanna, Predicting capillary absorption of porous stones by a procedure based on an intermingled fractal units model, Internat. J. Engrg. Sci. 82 (2014) 196–204.

[18] Z.L. Chen, N.T. Wang, L. Sun, X.H. Tan, S. Deng, Prediction method for permeability of porous media with tortuosity effect based on an intermingled fractal units model, Internat. J. Engrg. Sci. 121 (2017) 83–90.

[19] S. Pimenta, S.T. Pinho, An analytical model for the translaminar fracture toughness of fibre composites with stochastic quasi-fractal fracture surfaces, J. Mech. Phys. Solids 66 (2014) 78–102.

[20] J. Shi, A.H. Akbarzadeh, 3D hierarchical lattice ferroelectric metamaterials, Internat. J. Engrg. Sci. 149 (2020) 103247.

[21] Y.H. Zhang, H.R. Fu, S. Xu, J.A. Fan, K.C. Hwang, J.Q. Jiang, J.A. Rogers, Y.G. Huang, A hierarchical computational model for stretchable interconnects with fractal-inspired designs, J. Mech. Phys. Solids 72 (2014) 115–130.

[22] J.A. Fan, W.H. Yeo, Y. Su, et al., Fractal design concepts for stretchable electronics, Nature Commun. 5 (2014) 3266.

[23] L.R. Meza, A.J. Zelhofer, N. Clarke, A.J. Mateos, D.M. Kochmann, J.R. Greer, Resilient 3D hierarchical architected metamaterials, Proc. Natl. Acad. Sci. 112 (2015) 11502–11507.

[24] X.Y. Zheng, W. Smith, J. Jackson, et al., Multiscale metallic metamaterial, Nature Mater. 15 (2016) 1100–1106.

[25] B. Grigoryan, S.J. Paulsen, D.C. Corbett, et al., Multivascular networks and functional intravascular topologies within biocompatible hydrogels, Science 364 (2019) 458–464.

[26] A. Korolj, H.T. Wu, M. Radisic, A healthy dose of chaos: Using fractal frameworks for engineering higher-fidelity biomedical systems, Biomaterials (2019) 119363.

[27] N. Aage, E. Andreassen, B.S. Lazarov, O. Sigmund, Giga-voxel computational morphogenesis for structural design, Nature 550 (2017) 84–86.

[28] E. Andreassen, A. Clausen, M. Schevenels, B.S. Lazarov, O. Sigmund, Efficient topology optimization in MATLAB using 88 lines of code, Struct. Multidiscip. Optim. 43 (2011) 1–16.

[29] Z.L. Zhao, S.W. Zhou, X.Q. Feng, Y.M. Xie, On the internal architecture of emergent plants, J. Mech. Phys. Solids 119 (2018) 224–239.

[30] Z.Y. Ma, O. Stalnov, X. Huang, Design method for an acoustic cloak in flows by topology optimization, Acta Mech. Sinica 35 (2019) 964–971.

[31] M. Osanov, J.K. Guest, Topology optimization for architected materials design, Annu. Rev. Mater. Res. 41 (2016) 211–433.

[32] Y.Q. Wang, F.F. Chen, M.Y. Wang, Concurrent design with connectable graded microstructures, Comput. Methods Appl. Mech. Engrg. 317 (2017) 84–101.

[33] H.K. Zhang, Y.G. Wang, Z. Kang, Topology optimization for concurrent design of layer-wise graded lattice materials and structures, Internat. J. Engrg. Sci. 138 (2019) 26–49.

[34] K. Long, X. Wang, X.G. Gu, Concurrent topology optimization for minimization of total mass considering load-carrying capabilities and thermal insulation simultaneously, Acta Mech. Sinica 34 (2018) 315–326.

[35] B. Hassani, E. Hinton, A review of homogenization and topology optimization I-analysis and numerical solution of homogenization equations, Comput. Struct. 69 (1988) 719–738.

[36] O. Sigmund, Materials with prescribed constitutive parameters: an inverse homogenization problem, Int. J. Solids Struct. 31 (1994) 2313–2329.

[37] H.K. Zhang, Z. Kang, Y.Q. Wang, W.J. Wu, Isotropic "quasi-fluid" metamaterials designed by topology optimization, Adv. Theory Simul. 3 (2020) 1900182.

[38] W.H. Zhang, L.Y. Zhao, T. Gao, S.Y. Cai, Topology optimization with closed b-splines and boolean operations, Comput. Methods Appl. Mech. Engrg. 315 (2017) 652–670.

[39] D. Wang, W.H. Zhang, J.G. Yang, Z.P. Wang, A virtual punching method for shape optimization of openings on curved panels using CAD-based Boolean operations, Comput. Aided Des. 44 (2012) 388–399.

[40] B. Bourdin, Filters in topology optimization, Internat. J. Numer. Methods Engrg. 50 (2001) 2143–2158.

[41] H.K. Zhang, Y.J. Luo, Z. Kang, Bi-material microstructural design of chiral auxetic metamaterials using topology optimization, Compos. Struct. 195 (2018) 232–248.

[42] K. Svanberg, The method of moving asymptotes - a new method for structural optimization, Internat. J. Numer. Methods Engrg. 24 (1987) 359–373.

[43] R. Xia, X.Q. Feng, G.F. Wang, Effective elastic properties of nanoporous materials with hierarchical structure, Acta Mater. 59 (2011) 6801–6808.

[44] Y.Q. Wang, O. Sigmund, Quasiperiodic mechanical metamaterials with extreme isotropic stiffness, Extreme Mech. Lett. 34 (2020) 100596.

[45] T. Tancogne-Dejean, M. Diamantopoulou, M.B. Gorji, C. Bonatti, D. Mohr, 3D plate lattices: An emerging class of low density metamaterial exhibiting optimal isotropic stiffness, Adv. Mater. 30 (2018) 1803334.

[46] J.B. Berger, H.N.G. Wadley, M. MR, Mechanical metamaterials at the theoretical limit of isotropic elastic stiffness, Nature 543 (2017) 533–537.

[47] O. Sigmund, N. Aage, E. Andreassen, On the (non-)optimality of michell structures, Struct. Multidiscilinary Optim. 54 (2016) 361–373.